Rheology of ε-iron up to 19 GPa and 600 K in the D-DIA

Norimasa Nishiyama,[1,2] Yanbin Wang,[1] Mark L. Rivers,[1,3] Steve R. Sutton,[1,3] and David Cookson[4]

Received 28 July 2007; revised 9 October 2007; accepted 7 November 2007; published 7 December 2007.

[1] Stress-strain curves, i.e., relations between the differential stress and macroscopic sample strain, of polycrystalline ε-iron have been obtained at pressures of 17(±1) GPa, three different temperatures (600, 400, and 300 K), and various strain rates between 3.8×10^{-6} and 2.3×10^{-5} s^{-1} using the deformation-DIA coupled with monochromatic X-rays. Five independent stress-strain curves were obtained on axial shortening and the sample exhibited ductile behavior in all. Above 4% axial strain, sample stresses reach saturation and the sample exhibited steady-state deformation. Stress exponents at temperatures of 400 and 600 K were determined to be ~31 and ~7, respectively. These results indicate that ε-iron deforms in plasticity regime below 400 K and that the dominant deformation mechanism at 600 K may be low temperature power-law creep. The overall deformation behavior for ε-iron is consistent with that of zinc, suggesting that the deformation mechanism map of ε-iron resembles those of other hexagonal metals. **Citation:** Nishiyama, N., Y. Wang, M. L. Rivers, S. R. Sutton, and D. Cookson (2007), Rheology of ε-iron up to 19 GPa and 600 K in the D-DIA, *Geophys. Res. Lett.*, *34*, L23304, doi:10.1029/2007GL031431.

1. Introduction

[2] Hexagonal closed packed ε-iron has a wide stability field at pressure (P) and temperature (T) conditions corresponding to the Earth's inner core and serves as a reasonable starting point to model the rheology of the inner core. Seismological observations reveal the presence of seismic anisotropy in the inner core [e.g., *Poupinet et al.*, 1983] and it has been suggested that lattice preferred orientation (LPO) attained during deformation may be responsible for this anisotropy [e.g., *Wenk et al.*, 1988]. Several experimental studies carried out to investigate LPO developed during deformation [e.g., *Wenk et al.*, 2000] succeeded in determining the active slip system of ε-iron at high pressure [*Merkel et al.*, 2004]. However, to date, there have been no experimentally determined mechanical data for ε-iron defining the relationships between differential stress and strain at prescribed P, T, and strain rates.

[3] Recently, a new experimental technique has been developed using a combination of the deformation-DIA (D-DIA) and monochromatic synchrotron X-rays, enabling us to obtain quantitative mechanical data at pressure above 10 GPa [*Wang et al.*, 2003]. Using this technique, deformation experiment of ε-iron has been performed in its stability field in the present study. We report stress-strain curves for a polycrystalline ε-iron obtained at pressures of 17(±1) GPa and temperatures up to 600 K. The present mechanical data of ε-iron are compared with a deformation mechanism map of zinc, another hexagonal metal.

2. Experiment

[4] The deformation experiment was performed at the GSECARS bending magnet beamline 13-BM-D at the Advanced Photon Source (Argonne, IL, USA). We used the D-DIA with a monochromatic X-ray diffraction and a radiographic imaging system (for details see *Wang et al.* [2003] and *Uchida et al.* [2005]). Monochromatized X-rays at 65 keV (0.191 Å) were employed.

[5] We used four tungsten carbide and two sintered-diamond (SD) anvils with a truncated edge length of 2 mm which can generate pressures up to 20 GPa [*Yagi and Akimoto*, 1976]. The binder of the SD is silicon carbide (Ringwood Superabrasives, Australia), which is semitransparent to X-rays [*Irifune et al.*, 1998]. We used these SD anvils on the down-stream side in the D-DIA, to serve as windows for diffracted X-rays. Thus, we were able to observe diffraction Debye rings over the entire 360° detector azimuth range, perpendicular to the incident beam direction.

[6] The cell assembly used in the present study was similar to that described in the previous studies [e.g., *Uchida et al.*, 2005]. The starting material was an α-iron (bcc) rod (0.5 mm in diameter and 0.6 mm in length). The generated temperature was inferred from the input power using a power-temperature relation which had been determined in a separate run. We used similar cell assemblies for 'regular-DIA' experiments and the power vs. temperature relation was quite reproducible. We believe that the temperature uncertainty of the present study is less than ±50 K.

[7] Data reported here were collected in a single run. First, the cell assembly was pressurized isotropically up to a load of 50 T. At this load, the sample was still α-iron and the generated pressure of ~15 GPa was calculated using a P-V relation of α-iron determined by *Mao et al.* [1967]. At this fixed load, the sample was heated up to 700 K, and the phase transition from α- to ε-iron was observed by diffraction. After several minutes of heating at this temperature, α-iron had completely disappeared and the generated pressure was calculated using an equation of state of ε-iron [*Uchida et al.*, 2001] to be 14.5 GPa at 700 K. After the synthesis of ε-iron, five shortening-lengthening deformation cycles were performed by advancing and retracting

[1]Center for Advanced Radiation Sources, University of Chicago, Chicago, Illinois, USA.
[2]Now at Geodynamics Research Center, Ehime University, Matsuyama, Japan.
[3]Department of Geophysical Sciences, University of Chicago, Chicago, Illinois, USA.
[4]Australian Synchrotron Research Program, Argonne, Illinois, USA.

0094-8276/07/2007GL031431

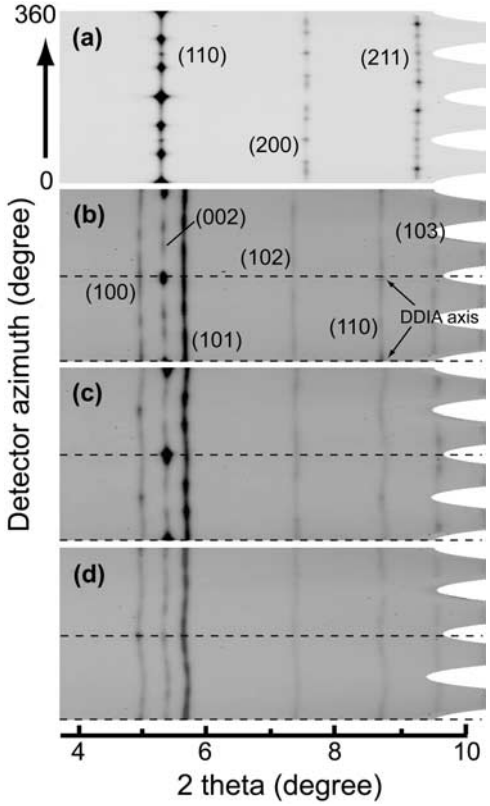

Figure 1. Representative X-ray diffraction patterns (a) Starting material (α-iron) at ambient conditions, (b) $P = 14.5$ GPa and $T = 700$ K just after complete transition to ε-iron, (c) $P = 17$ GPa and $T = 600$ K during shortening ($\sigma_a > \sigma_r$, $\sigma_a = \sigma_1$ and $\sigma_r = \sigma_2 = \sigma_3$), (d) $P = 13$ GPa and $T = 600$ K during lengthening ($\sigma_a < \sigma_r$, $\sigma_a = \sigma_3$ and $\sigma_r = \sigma_1 = \sigma_2$). The shortening and lengthening axis of the sample by D-DIA (DDIA axis) is at the detector azimuth of 0° and 180°, which is shown as dashed lines.

the differential ram pistons at various speeds. The first and second cycles were carried out at 600 K, the third and fourth at 400 K, and the fifth was at room temperature. In each cycle, an average strain rate, $\langle\dot{\varepsilon}\rangle$, was calculated based on sample length measurements during deformation.

[8] Methods of data analysis were based on those described elsewhere [*Uchida et al.*, 2004; *Duffy et al.*, 1999]. Three reflections, (100), (002), and (101), were used for the analyses. We fitted the measured d-spacing, $d_m(hkl)$, to the following equation: $[d_m(hkl) - d_P(hkl)]/d_P(hkl) = \varepsilon_t(hkl)(1-3\cos^2\varphi)$, where φ is the true azimuth angle, given by $\cos\varphi = \cos\theta\cos\chi$ (θ and χ are the diffraction angle and detector azimuth), and $d_P(hkl)$ is the d-spacing under the equivalent hydrostatic pressure. $d_P(hkl)$ was determined at $\varphi = 54.7°$ and the equivalent angles, where $(1-3\cos^2\varphi) = 0$. Using the $d_P(hkl)$, the unit cell parameters were determined and the hydrostatic pressure was calculated using an equation of state of ε-iron [*Uchida et al.*, 2001] In order to see the detector azimuth dependence of $d_m(hkl)$, we used a software package, saxs15id, developed at ChemMatCARS, the University of Chicago [*Cookson et al.*, 2006] (the software package is available at http://cars.uchicago.edu/chemmat). Here, the direction of $\chi = 0°$ (and 180°) corresponds to the shortening (and lengthening) direction.

[9] We defined the macroscopic sample differential stress ($t = \sigma_a - \sigma_r$, where σ_a and σ_r are the stresses in the axial (vertical) and radial (horizontal) directions of the sample, respectively) by averaging differential stresses calculated from the available reflections *hkl*: $t(hkl) = 6\varepsilon_t(hkl)G(hkl)$, where $G(hkl)$ is the appropriate modulus of aggregate, which is calculated using single crystal elastic moduli [e.g., *Weidner et al.*, 2004; *Merkel et al.*, 2005]. Since experimental data of the single crystal elastic moduli of hcp-iron are limited [e.g., *Mao et al.*, 1998; *Merkel et al.*, 2005], we used those determined by first-principles calculations [*Vocadlo et al.*, 2003]. The total sample axial strain was calculated using $\varepsilon_{total} = (l_0\text{-}l)/l_0$, where l is the sample length measured during deformation, and l_0 is the reference length, which can be determined for each deformation cycle.

3. Results and Discussion

[10] Representative X-ray diffraction patterns, converted from the original form in polar coordinates into Cartesian systems, are shown in Figure 1, where high intensities are represented by the darkness. Figure 1a shows a diffraction pattern of the starting sample, which is α-iron, at ambient conditions. The positions of each diffraction line exhibit no χ dependence indicting the absence of differential stress. There is strong intensity variation with χ, indicating lattice preferred orientation (LPO), because the starting sample was a polycrystalline fragment from an iron wire. The preferred orientation may be developed during manufacture. Figure 1b is a pattern collected just after the synthesis of ε-iron at 700 K. Weak χ dependence of the peak positions are observed (two maxima at $\chi \sim 0°$ and 180°) indicating that $\sigma_a > \sigma_r$. Figures 1c and 1d are patterns collected during shortening and lengthening, respectively, in the first deformation cycle at 600 K. In Figure 1, the peak position of every diffraction line clearly varies with χ. There are two maxima at $\chi \sim 0°$ and 180° in Figure 1c, indicating $\sigma_a > \sigma_r$, thus, $\sigma_a = \sigma_1$ and $\sigma_r = \sigma_2 = \sigma_3$. In Figure 1d, the peak position of every diffraction line shows minima at these χ, indicating $\sigma_a < \sigma_r$, thus, $\sigma_a = \sigma_3$ and $\sigma_r = \sigma_1 = \sigma_2$. In Figure 1, we can also observe intensity variations with χ. In Figure 1c (under shortening), the (100) reflection shows intensity maxima at $\chi \sim 90°$ and 270°, while the (002) peak has intensity maxima at $\chi \sim 0°$ and 180°. These intensity variations are similar to those observed in previous studies performed using diamond anvil cell [*Wenk et al.*, 2000; *Merkel et al.*, 2004], suggesting that the dominant deformation mechanisms under shortening are $(0001)\langle\bar{1}2\bar{1}0\rangle$ basal slip and $\{10\bar{1}0\}\langle\bar{1}2\bar{1}0\rangle$ prismatic slip [*Merkel et al.*, 2004], when the sample was under shortening. On the other hand, the intensity variations observed in Figure 1d (under lengthening) are different from those in Figure 1c. For example, (100) shows intensity maxima at $\chi \sim 0°$ and 180°. The change in intensity variation with χ between shortening and lengthening was observed in all the deformation cycles reproducibly.

[11] In the first deformation cycle, the reference sample length (l_0) was defined as the sample length at the very

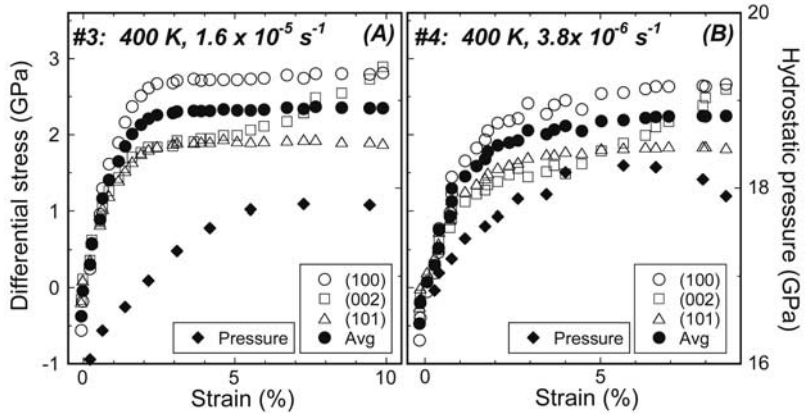

Figure 2. Representative stress-strain curves of ε-iron and strain rate dependence of ultimate strength. (a) The third shortening segment at 50 tons and 400 K. $\langle\dot{\varepsilon}\rangle = 1.6 \times 10^{-5}$ s^{-1} and pressure at steady-state flow is about 18 GPa. (b) The fourth shortening segment at 50 tons and 400 K. $\langle\dot{\varepsilon}\rangle = 3.8 \times 10^{-6}$ s^{-1} and pressure at steady-state flow is about 18 GPa. Hydrostatic pressure reaches saturation at $\varepsilon_{total} \sim 6\%$. Ultimate strength (see text) increases with strain rate.

beginning of deformation to calculate the total sample strain, whereas in the other cycles, the sample lengths at $t = (\sigma_a - \sigma_r) = 0$ in the shortening segments were taken as l_0. Five stress-strain curves, i.e., the relation between differential stress (t) versus total strain (ε_{total}), were obtained in the five shortening segments during deformation cycles at three different temperatures (300, 400, and 600 K), and various strain rates (3.8×10^{-6}–2.3×10^{-5} s^{-1}). The lengthening segments were only used to release differential stress for the next shortening segment.

[12] Figures 2a and 2b show stress-strain curves observed in the third and fourth shortening segments, respectively. The *PT* conditions of these curves are almost identical (17 GPa and 400 K, see Table 1), while $\langle\dot{\varepsilon}\rangle$ of the third shortening segment was more than four times higher than that of the fourth. In Figure 2, differential stresses calculated from the three different peaks have similar values, increasing linearly with strain up to $\varepsilon_{total} \sim 1\%$, where the stress values start diverging and the curves start deviating from linearity. We define this deviation point as the yield point [*Uchida et al.*, 2004]. Beyond the yield point, stress values of (100) are larger than those of (101) but the behaviors of the stress-strain curves of these two reflections are similar; differential stresses increase non-linearly with ε_{total} (transient creep) and, eventually, reach saturations at $\varepsilon_{total} \sim 4\%$, where the sample starts deforming in steady-state flow. The difference between stress values of (002) and (101) is small up to $\varepsilon_{total} \sim 4\%$; where the differential stress of (002) starts increasing again immediately after the attainment of steady-state flow. We observed this behavior in all the stress-stain curves obtained in the present study. This behavior might be related to dominant deformation mechanism, contributing to the development of LPO. Further texture studies are needed to investigate the deformation mechanism of ε-iron using the diffraction patterns obtained in the present study. The technique is available and described elsewhere [e.g., *Merkel et al.*, 2004]. In the present study, we determined the sample stress by averaging stresses calculated using (100) and (101) reflections. We refer to the sample stress after the attainment of steady-state flow as the ultimate strength. As observed in Figures 2a and 2b, ultimate strength increases with strain rate at these *PT* conditions.

[13] Table 1 summarizes the ultimate strengths determined for all the deformation cycles. As shown in Table 1, we obtained ultimate strengths at two different strain rates at 600 and 400 K, respectively. Pressure listed in Table 1 is the averaged pressure throughout entire deformation segment. The pressures of the five deformation segments are 17.0 ± 1.1 GPa. Thus we presumed the ultimate strengths determined in the present study to be obtained at a constant pressure of 17 GPa. At a certain pressure and temperature, strain rate dependence of ultimate strength can be fitted to $\dot{\varepsilon} = A\ \sigma_u^n$ where A is a constant, $\dot{\varepsilon}$ strain rate, σ_u ultimate strength, and n the stress exponent. We obtained $n \sim 7$

Table 1. Temperatures, Pressures, Strain Rates, Ultimate Strengths (σ_u), and Determined Stress Exponents (n) of ε-Fe[a]

Cycle	Temperature, K	Pressure, GPa	Strain Rate, 10^{-5} s^{-1}	σ_u Average, GPa	σ_u-100, GPa	σ_u-101, GPa
1	600	15.9(9)	2.27(9)	2.1(1)	2.4(1)	1.7(1)
2	600	17.0(3)	0.87(9)	1.8(1)	2.0(1)	1.5(1)
				n ∼ 7	n ∼ 5	n ∼ 10
3	400	17.0(7)	1.59(7)	2.3(1)	2.8(1)	1.9(1)
4	400	17.5(7)	0.38(2)	2.2(1)	2.6(1)	1.8(1)
				n ∼ 31	n ∼ 28	n ∼ 35
5	300	18.1(12)	1.11(3)	2.5(1)	2.9(1)	2.0(1)

[a]Pressure and Strain Rate are the averaged pressure and strain rate, respectively, throughout entire deformation segment. σ_u-avg: ultimate strength of averaged differential stress of (100) and (101); σ_u-100: ultimate strength determined by (100) reflection; σ_u-101: ultimate strength determined by (100) reflection. Stress exponents (n) were determined using isothermal data (600 K and 400 K).

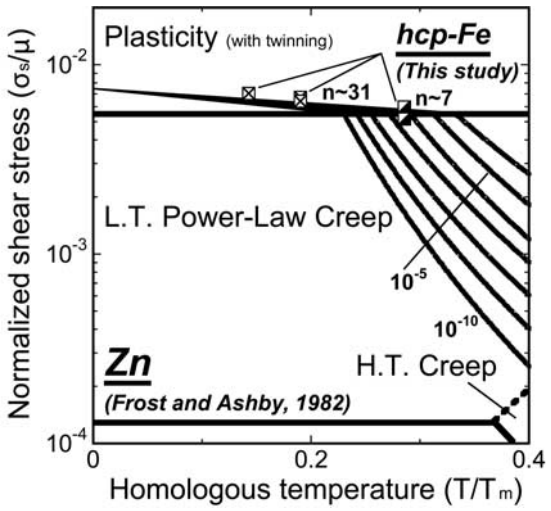

Figure 3. Comparison between steady-state mechanical data of ε-iron and the deformation mechanism map of zinc with a grain size of 0.1 mm [*Frost and Ashby*, 1982]. Squares with cross and half-closed squares represent mechanical data of ε-iron obtained at T below 400 K and at 600 K, respectively. For the data of ε-iron, μ (shear modulus) at 17 GPa was calculated using those determined by first-principles calculations [*Vocadlo et al.*, 2003], and T_m at 17 GPa determined by *Shen et al.* [1998] was employed. The overall behavior of the mechanical data for ε-iron obtained in the present study is consistent with the deformation mechanism map of zinc, which is the one of the hexagonal metals.

and ~31 at temperatures of 600 and 400 K, respectively. The n-values can be determined using ultimate strengths determined by (100) and (101) reflections and, in any case, n-values at 400 K are much larger than those at 600 K. The large difference in n-values determined at these temperatures indicates that the deformation mechanism at 600 K is different from that at 400 K.

[14] Figure 3 compares the steady-state mechanical data of ε-iron obtained in the present study with the deformation mechanism map of zinc, which is one of the hexagonal metals, with a grain size of 0.1 mm [*Frost and Ashby*, 1982]. In order to plot the present data on this map, we calculated normalized shear stress, σ_s/μ where $\sigma_s = (\sigma_1 - \sigma_3)/\sqrt{3}$ [*Frost and Ashby*, 1982] and μ is shear modulus, and homologous temperature, T/T_m (T_m is melting temperature). To compare isobaric data at 17 GPa, we employed the shear modulus of 173 GPa, which was interpolated from those at various pressures determined by first-principles calculations [*Vocadlo et al.*, 2003]. Temperature effect on the shear modulus was ignored. For the melting temperature of iron at this pressure, we employed T_m = 2100 K determined by *Shen et al.* [1998]. The mechanical data points of ε-iron at 300 and 400 K are in the region where the deformation mechanism of low-temperature plasticity is dominant for zinc, whereas the data points at 600 K are at the boundary between the regions of plasticity and of low temperature power-law creep. The abnormally large stress exponent (n ~ 31) at 400 K for ε-iron is consistent with the insensitivity to strain rate in the ultimate strength and low-temperature plasticity behavior under these conditions; for zinc, n > 80 can be calculated using parameters to describe this deformation mechanism [*Frost and Ashby*, 1982]. According to *Frost and Ashby* [1982], n = 4.5 was employed for high temperature power-law creep when they constructed this map for zinc. Although there has been no data for pure zinc which lie in the low temperature power-law regime, *Edwards* [1971] obtained data in this regime using powder-metallurgy zinc containing 1.2 vol% of ZnO. The data are consistent with n ~ 6. Therefore, the present data obtained for ε-iron at 600 K (n ~ 7) may lie in the low temperature power-law regime. The overall deformation behavior for ε-iron is consistent with that of zinc, suggesting that the deformation mechanism map of ε-iron resembles those of other hexagonal metals.

[15] **Acknowledgments.** We thank N. Lazarz, F. Sopron, M. Jagger, and GSECARS personnel for their support for the experiment. We also thank two anonymous reviewers to review this paper. GeoSoilEnviroCARS is supported by the National Science Foundation–Earth Sciences (EAR-0622171), and Department of Energy–Geosciences (DE-FG02-94ER14466). Use of the Advanced Photon Source was supported by the U. S. Department of Energy, Office of Science, Office of Basic Energy Sciences, under contract DE-AC02-06CH11357. N.N is partly supported by Postdoctoral Fellowships for Research Abroad of Japan Society for the Promotion of Science.

References

Cookson, D. J., N. Kirby, R. Knott, M. Lee, and D. Schultz (2006), Strategies for data collection and calibration on the small angle X-ray scattering camera at ChemMatCARS, Advanced Photon Source, *J. Synchrotron Radiat.*, *13*, 440–444.

Duffy, T. S., G. Shen, D. L. Heinz, J. Shu, Y. Ma, H. K. Mao, and R. J. Hemley (1999), Lattice strains in gold and rhenium under nonhydrostatic compression to 37 GPa, *Phys. Rev. B*, *60*, 15,063–15,073.

Edwards, G. R. (1971), The mechanical behavior of powder metallurgy zinc and zinc-tungsten particulate composites, Ph.D. thesis, Stanford Univ., Stanford, Calif.

Frost, H. J., and M. F. Ashby (1982), *Deformation-Mechanism Maps*, pp. 108–110, Pergamon, Oxford, U. K.

Irifune, T., et al. (1998), X-ray diffraction measurements in a double stage multianvil apparatus using ADC anvils, in *Properties of Earth and Planetary Materials at High Pressure and Temperature*, *Geophys. Monogr. Ser.*, vol. 101, edited by M. H. Manghnani and T. Yagi, pp 1–8, AGU, Washington, D. C.

Mao, H. K., W. A. Bassett, and T. Takahashi (1967), Effect of pressure on crystal structure and lattice parameters of iron up to 300 kbars, *J. Appl. Phys.*, *38*, 272–276.

Mao, H. K., J. Shu, G. Shen, R. J. Hemley, B. Li, and A. K. Singh (1998), Elasticity and rheology of iron above 220 GPa and the nature of the Earth's inner core, *Nature*, *369*, 741–743.

Merkel, S., H. R. Wenk, P. Gillet, H. K. Mao, and R. J. Hemley (2004), Deformation of polycrystalline iron up to 30 GPa and 1000 K, *Phys. Earth Planet. Inter.*, *145*, 239–251.

Merkel, S., J. Shu, P. Gillet, H.-K. Mao, and R. J. Hemley (2005), X-ray diffraction study of the single-crystal elastic moduli of ε–Fe up to 30 GPa, *J. Geophys. Res.*, *110*, B05201, doi:10.1029/2004JB003197.

Poupinet, G., R. Pillet, and A. Souriau (1983), Possible heterogeneity of the Earth's inner core deduced from PKIKP travel times, *Nature*, *305*, 204–206.

Shen, G., H. Mao, R. J. Hemley, T. S. Duffy, and M. L. Rivers (1998), Melting and crystal structure of iron at high pressures and temperatures, *Geophys. Res. Lett.*, *25*, 373–376.

Uchida, T., Y. Wang, M. L. Rivers, and S. R. Sutton (2001), Stability field and thermal equation of state of ε-iron determined by synchrotron X-ray diffraction in a multi-anvil apparatus, *J. Geophys. Res.*, *106*, 21,799–21,810.

Uchida, T., Y. Wang, M. L. Rivers, and S. R. Sutton (2004), Yield strength and strain hardening of MgO up to 8 GPa measured in the deformation-DIA with monochromatic X-ray diffraction, *Earth Planet. Sci. Lett.*, *226*, 117–126.

Uchida, T., Y. Wang, M. L. Rivers, and S. R. Sutton (2005), Stress and strain measurements of polycrystalline materials under controlled deformation at high pressure using monochromatic synchrotron radiation, in

Advances in High-Pressure Technology for Geophysical Applications, edited by J. Chen et al., chap. 7, pp. 137–165, Elsevier, New York.

Vocadlo, L., D. Alfe, M. J. Gillan, and G. D. Price (2003), The properties of iron under core conditions from first principles calculations, *Phys. Earth Planet. Inter.*, *140*, 101–125.

Wang, Y., W. B. Durham, I. C. Getting, and D. J. Weidner (2003), The deformation-DIA: A new apparatus for high temperature triaxial deformation to pressures up to 15 GPa, *Rev. Sci. Instrum.*, *74*, 3002–3011.

Weidner, D. J., L. Li, M. Davis, and J. Chen(2004), Effect of plasticity on elastic modulus measurements, *Geophys. Res. Lett.*, *31*, L06621, doi:10.1029/2003GL019090.

Wenk, H. R., T. Takeshita, R. Jeanloz, and G. C. Johnson (1988), Development of texture and elastic anisotropy during deformation of hcp metals, *Geophys. Res. Lett.*, *15*, 76–79.

Wenk, H. R., S. Matthies, R. J. Hemley, H. K. Mao, and J. Shu (2000), The plastic deformation of iron at pressures of the Earth's inner core, *Nature*, *405*, 1044–1047.

Yagi, T., and S. Akimoto (1976), Pressure fixed points between 100 and 200 kbar based on the compression of NaCl, *J. Appl. Phys.*, *47*, 3350–3354.

D. Cookson, Australian Synchrotron Research Program, Building 434, 9700 South Cass Avenue, Argonne, IL 60439, USA. (cookson@cars.uchicago.edu)

N. Nishiyama, Geodynamics Research Center, Ehime University, 2-5 Bunkyo-cho, Matsuyama 790-8577, Japan. (nishiyama@sci.ehime-u.ac.jp)

M. L. Rivers, S. R. Sutton, and Y. Wang, Center for Advanced Radiation Sources, University of Chicago, 5640 South Ellis Avenue, Chicago, IL 60637, USA. (rivers@cars.uchicago.edu; sutton@cars.uchicago.edu; wang@cars.uchicago.edu)